nature communications

Article

https://doi.org/10.1038/s41467-026-78042-6

Fast-charging and durable all-solid-state lithium-sulfur batteries enabled by pre-embedded solid-solid redox mediator

Received: 8 June 2026

Accepted: 10 September 2026

Published online: 09 October 2026

Check for updates

Huimin Song[1], Ruizhuo Zhang[2], Chenxi Zheng[3], Konrad Münch[4], Kaier Shen[1], Fang Liu[5], Xufeng Hong[1], Hong Wang[5], Jiashen Meng[1], Yingjing Yan[1], Weize Shi[1], Mengxue He[1], Yue Ma[1], Yitao Li[1], Zhitong Xiao[1], Muhammad Burhan Shafqat[1], Xin Gao[1], Jinsong Wu[5], Mingchuan Luo[1], Tinglu Song[6], Chenyan Ma[7], Lei Zheng[7], Peng Gao[3], Mohammadhosein Safari[8], Yu Wang[9], Philip Henkel[2], Jürgen Janek[4], Torsten Brezesinski[2] & Quanquan Pang[1]

All-solid-state lithium-sulfur batteries promise high specific energy and low cost. However, they are challenged by poor rate capability and cycling stability owing to the slow solid-solid sulfur redox reactions. Here, we present fast-charging and durable all-solid-state lithium-sulfur batteries enabled by a pre-embedded solid-solid redox mediator using an amorphous sulfur/iodine nano-eutectic positive electrode. The iodine, intimately homogenized with sulfur owing to carbon mesopore encapsulation, undergoes rapid I_2/I^- redox reaction, mediating solid-solid sulfur reactions by promoting electron transfer across the boundaries. The iodine within the carbon and on its surface reacts in situ with the sulfide catholyte to form a globally distributed I_2/I^- nano-network throughout the positive electrode, thereby enabling fast charging. The cell exhibits a specific capacity of 851.9 mA h $g^{-1}_{S/I}$ when charged at 10 C, and 474.7 mA h $g^{-1}_{S/I}$ at a charging rate of 24 C (1 C is defined as 945 mA $g^{-1}_{S/I}$). The high reversibility of the redox-mediated reaction enables durable cycling for 9,000 cycles over 9 months at 2 C and 2,800 cycles over 17 months at 0.5 C. This strategy represents a perspective for developing solid-state conversion electrodes that are plagued by sluggish reactions.

Lithium-sulfur (Li-S) batteries remain competitive in promising high-energy and cost-effective energy storage[1–5]. Efforts on improving conventional Li-S batteries using liquid electrolytes (LEs) for the past decades are compromised by the notorious polysulfide shuttle phenomenon, and it turns out to be more challenging than anticipated to simultaneously achieve high cell-level specific energy and cycling stability[6–10]. In addition, LEs are susceptible to thermal runaway at high temperatures, posing great safety risks[5–7]. All-solid-state lithium-sulfur batteries (ASSLSBs) using solid electrolytes (SEs) not only promise high thermal safety[11–13], but also fundamentally eliminate the polysulfide shuttle challenge and promise higher cell-level specific energy by allowing a bipolar cell configuration[14–17]. Furthermore, ASSLSBs exhibit greater intrinsic safety than other all-solid-state batteries based on high-voltage layered metal oxide (LMO) electrodes, as sulfur electrodes are free of releasing active oxygen at high potentials, which is considered a major issue in all-solid-state LMO-based batteries[18].

However, ASSLSBs have not been explored in great depth as they suffer from poor solid-solid sulfur reaction kinetics at the positive electrode[5,7,8,10,14–16]. In principle, given the electron/ion-insulating

A full list of affiliations appears at the end of the paper. e-mail: qqpang@pku.edu.cn

nature of the main sulfur species (S_8 and Li_2S; Li_2S_x, if present), the in-particle transport and between-particle transfer of charge for solid-solid sulfur reactions are largely retarded[16,19–22]. Further, the substantial volume breathing of sulfur during discharge/charge can lead to mechanical contact failure and thereby degradation of the electron/ion conducting paths within the electrode[14,19,20].

Composite electrode engineering represents the primary effort to overcome the challenges of the poor solid-solid sulfur reaction kinetics and the solid-solid contact issues. This was achieved by mechanical milling or liquid-assisted compositing of active materials, electronic conductors and SEs[16,17,23–27]. Li_2S has been largely used as the starting active material, as it is synthetically more feasible to incorporate a range of functional additives, such as $LiVS_2$, LiI and carbons[28–30], to improve the sulfur utilization and cycling stability. Adding LiI to the Li_2S positive electrode has been shown to effectively improve the utilization of Li_2S, attributed to the improved ion transport by the ion-conducting LiI[31]. The effort discovered a molecular $S_{9.3}I$ electrode material which shows greatly increased electronic conductivity, resulting in prolonged cycling for 400 cycles[32]. Despite the greatly improved electron/ion conductivities of positive electrode materials, the rate and cycling stability of ASSLSBs are generally inferior to intercalation-based batteries (Supplementary Table S1)[11–13,19,33–35]. This drives us to revisit the solid-solid sulfur redox reactions by exploring effects beyond the mere improvement of charge transport capabilities.

For solid-solid conversion reactions to occur, the electrons must be transferred to the active material surface across the solid-solid carbon|active material boundaries, and simultaneously Li^+ ions must be transferred to the active material surface across the solid-solid SE|active material boundaries. In other words, solid-solid conversion reactions can only occur at multi-phase boundaries[14–16]. However, the spatial density of all-solid multi-phase boundaries (MPB) and the density of corresponding MPB sites is typically much lower than the density of sites at bi-phase boundaries available in LE-based batteries[5–7,36–38], and surely lower than that in LMO-based batteries as LMOs are mostly well electron-conducting[11–13,39–41]. To make it worse, solid-solid conversion reactions must not simply occur at the surface of the active material but have to propagate to the bulk of the active material particles, which involves long-range migration of Li^+/electrons for large-grained active materials[16,17]. One representative situation as such has been the charging of Li/Na-O_2 batteries that are challenged by oxidation of large electron/Li^+-insulating Li_2O_x/Na_2O_x particles; this has been largely resolved by redox mediation strategies[42–45]. Nevertheless, in those cases, the redox mediators are present as dissolved molecules in the LEs, allowing them to diffuse to the reaction sites[44,46,47]. Recent reports on using redox-active $LiVS_2$ and solid electrolyte for ASSLSBs to realize such a concept are fruitful in the all-solid-state configuration[29,48]. However, unlike the dissolved redox mediators in LEs, which exhibit sufficient liquid-solid contact with the active materials, the nature of introducing these redox mediators as an additional solid phase fundamentally limits the number of sulfur −mediator phase boundaries for the charge transfer and reactions to occur. A fundamental question remains as to how to establish effective solid-solid contact for such an effect to take place, particularly for high-fraction and high-loading positive electrodes.

Herein, we describe a solid-solid redox mediation (SSRM) strategy that transforms the sluggish boundary-demanding sulfur reaction to a boundary-cooperative sulfur reaction that is rapid, reversible and spatially improved by a pre-embedded solid-solid redox mediator (PE-SSRM). In the amorphous sulfur-iodine nanocomposite, presented below, with a nominal eutectic stoichiometry of S_8I_2, the iodine is intimately homogenized with sulfur on the nanometer scale owing to confinement by mesoporous carbon black. The iodine undergoes redox reactions via the I_2/I^- couple and serves to redox-mediate the solid-solid sulfur reaction. The nanometric homogenization lays the foundation to amplify the SSRM effect by maximizing the spatial density of mediation and reaction sites. Further, a fraction of the I_2 within and on the surface of the porous carbon in situ reacts with the sulfide catholyte to form LiI, leading to a globally distributed I^-/I_2 network through the positive electrode. Through PE-SSRM, the ASSLSBs exhibit good charging rate performance, showing a high capacity of 851.9 mA h $g^{-1}_{S/I}$ (specific capacities and rates based on the total mass of S_8I_2 material, noted as S/I, hereafter) at a charging rate of 10 C (10.4 mA cm^{-2}), while maintaining 474.7 mA h $g^{-1}_{S/I}$ even at 24 C (24.9 mA cm^{-2}, 25 °C). The cell with a high fraction of up to 70 wt% active material in the positive electrode shows durable cycling stability for 800 cycles with marginal capacity fade. With the demonstrated performances of high-fraction and high-loading positive electrodes, our work goes beyond the strategy of improving electron/Li^+ transport and offers a new perspective for curtailing the interfacial challenges of all-solid-state conversion-based electrodes.

Results

Design of the PE-SSRM

Although elemental sulfur and iodine possess very different structures at ambient temperature, they are miscible at elevated temperatures over a wide range of compositions[49], featuring a eutectic melt of S_8I_2 stoichiometry with a low melting point of 67.8 °C as determined from differential scanning calorimetry (Supplementary Figs. 1a, b). The co-condensation of S_8 and I_2 from a supercooled melt might result in a rather homogeneous S-I_2 solid solution or nanoscale composite (as shown below), which leads to a high density of solid-solid contact sites and promotes possible chemical interaction between the two. Further, as the redox potential of I^-/I_2 (2.8 V vs. Li^+/Li) is higher than that of Li_2S/S (2.2 V vs. Li^+/Li)[50], I^-/I_2 may serve as a redox mediator for the charging reaction in ASSLSBs from the thermodynamic point of view.

The composite with the eutectic stoichiometry of S_8I_2 is synthesized by heating the S-I_2 elemental mixture at 80 °C, forming a liquid melt, followed by natural cooling. The powder X-ray diffraction (XRD) pattern and Raman spectrum of the S_8I_2 composite confirm the presence of α-S_8 and I_2 as separated crystalline phases instead of a single phase (Fig. 1a and Supplementary Fig. 1c), which can be attributed to the different solidification kinetics and lattice mismatch of the two phases, i.e., a typical eutectic. This is further confirmed by cryo-transmission electron microscopy (TEM) imaging and selected area electron diffraction (SAED), which clearly show the presence of pure α-S_8 and I_2 (Supplementary Figs. 1d, e). The phase-separated crystalline S_8I_2 eutectic shows a lamellar texture on a scale of tens of microns, as widely observed for eutectic alloys and polymers (Fig. 1b)[51,52].

By employing a mesoporous carbon black, Ketjenblack (KB) here, as a framework for nano-encapsulation, the eutectic S_8I_2 melt solidifies into an amorphous phase (denoted as S_8I_2/KB), as confirmed by XRD patterns, TEM images and SAED patterns (Fig. 1a and Supplementary Figs. 2a, b). This finding contrasts with the formation of crystalline sulfur for the pure-sulfur counterpart (S/KB); the carbon-encapsulated iodine also shows an amorphous phase (I_2/KB) (Fig. 1a). These results indicate that the incorporation of iodine, combined with the spatial confinement from the nanocarbon - both materials are nonpolar and have an affinity to sulfur - alters the sulfur vitrification behavior and results in an amorphous phase during condensation. The high-angle annular dark-field scanning transmission electron microscopy (HAADF-STEM) image and the energy dispersive X-ray (EDX) spectroscopy analysis reveal that amorphous sulfur and iodine are homogeneously distributed at the nanometer scale in the eutectic S_8I_2/KB nanocomposite (Fig. 1d and Supplementary Fig. 2d). The S K-edge X-ray absorption near edge structure (XANES) spectra show that sulfur is present as elemental S^0 in S_8I_2/KB, and the much-reduced self-absorption (i.e., higher "white-line" intensity, 2472.7 eV) compared to that of S/KB indicates a much smaller sulfur grain size in the presence of iodine in the mesopores (Fig. 1c). We hypothesize that nanocarbon confinement hinders the long-range cross-diffusion of sulfur/iodine

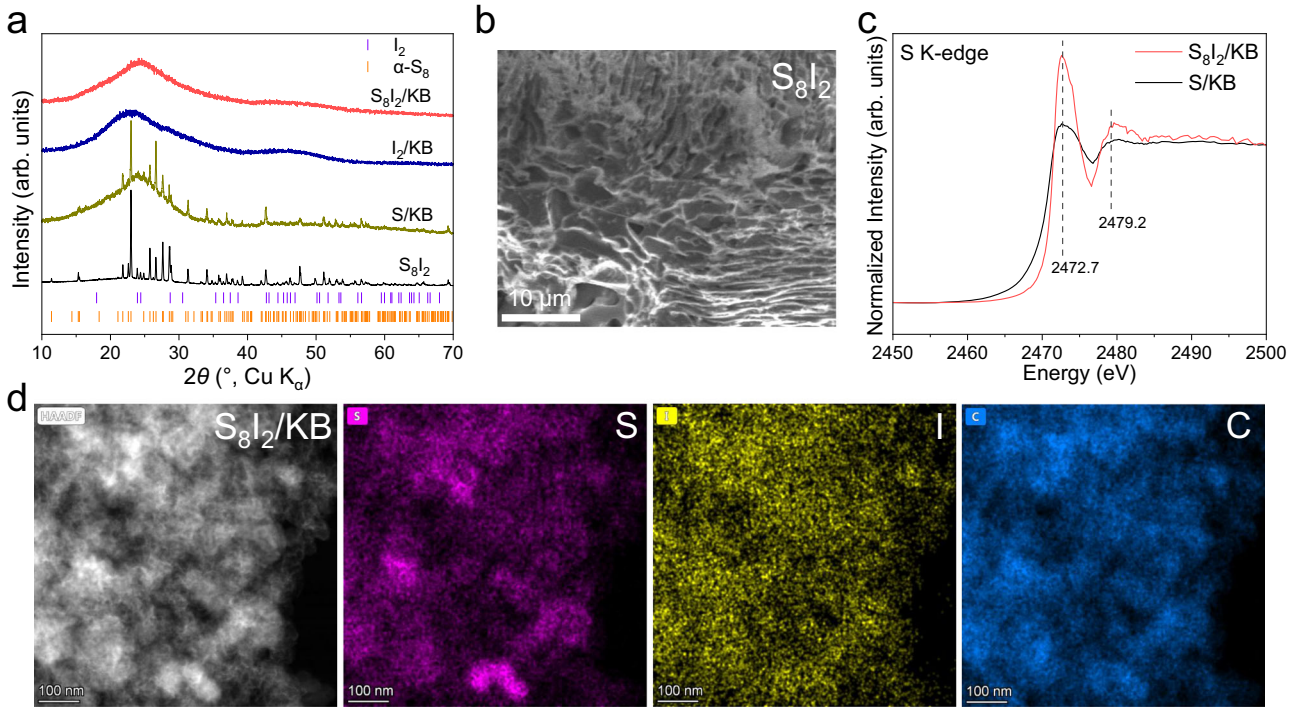


Fig. 1 | Characterization of the pre-embedded solid-solid redox mediator in the eutectic S_8I_2 nanocomposite. a X-ray diffraction patterns of S_8I_2 (non-carbon-encapsulated), S/KB, I_2/KB, and S_8I_2/KB wherein the weight ratio of KB is kept the same at 25 wt%; the *Bragg* diffraction peaks of α-S_8 and I_2 are listed at the bottom. **b** Scanning electron microscopy image of non-carbon-encapsulated S_8I_2 showing a lamellar texture on the scale of tens of microns. **c** S K-edge X-ray absorption near edge structure spectra of S/KB and S_8I_2/KB with the labeled white line at 2472.7 eV. **d** The high-angle annular dark-field scanning transmission electron microscopy image and the corresponding energy dispersive X-ray mapping of S_8I_2/KB.

and leads to amorphization as well as nanometric homogenization, which is foundational for amplifying the redox mediation effect of I^-/I_2 on the solid-solid sulfur reaction by increasing the density of mediation sites as illustrated below.

The fast-charging capability at 25 °C

We evaluate the charging rate capability of ASSLSBs using positive electrodes prepared by milling of the amorphous S_8I_2/KB eutectic with sulfide-SE catholyte and carbon (see "**Methods**"). We assembled cells with three common sulfide solid catholytes, *i.e.*, $Li_{5.5}PS_{4.5}Cl_{1.5}$, Li_3PS_4, and $Li_7P_3S_{11}$ (synthesis details in "**Methods**"), to demonstrate the impact of the amorphous S_8I_2/KB eutectic and to clarify the origin of the fast reaction kinetics as shown below. $Li_{5.5}PS_{4.5}Cl_{1.5}$ is used as the separator electrolyte against the In/InLi negative electrode. The cells are evaluated by charging at rates from 1 C to 24 C with a constant discharging rate of 2 C at 25 °C. The theoretical specific capacity of stoichiometric S_8I_2 is calculated to be 945 mA h $g^{-1}_{S/I}$, and thus, 1 C is defined as 945 mA $g^{-1}_{S/I}$ (note: 1672 mA h g^{-1}_{sulfur} for pure sulfur).

The S_8I_2/KB cell with $Li_{5.5}PS_{4.5}Cl_{1.5}$ catholyte exhibits a high specific capacity of 1132.5 mA h $g^{-1}_{S/I}$ at 1 C (1.0 mA cm^{-2}), and maintains a capacity of 851.9 mA h $g^{-1}_{S/I}$ at a high charging rate of 10 C (10.4 mA cm^{-2}) (Fig. 2a). Even at a charging rate of 24 C (24.9 mA cm^{-2}), the cell still demonstrates a high capacity of 474.7 mA h $g^{-1}_{S/I}$. Both the voltage profiles and differential capacity plots confirm well-defined plateaus and non-capacitive faradaic behavior at all charging rates, indicating the fast solid-solid sulfur reaction kinetics (Fig. 2b, d). In contrast, the cell with a pure sulfur (S/KB) composite, while exhibiting a high capacity of 1318.5 mA h g^{-1}_{sulfur} when charged at 1 C (1.7 mA cm^{-2}), maintains only 341.0 and 128.2 mA h g^{-1}_{sulfur}, respectively, when charged at 10 C (16.7 mA cm^{-2}) and 24 C (40.1 mA cm^{-2}) (discharged at 1 C, Fig. 2a, c, e). Note that the two cells show capacities higher than the theoretical values during the first activation cycles at low rates of 0.1-0.2 C; this is attributed to the capacity contribution from the redox reaction of the $Li_{5.5}PS_{4.5}Cl_{1.5}$ catholyte (discussed below)[39,53]. The cell with an S_8I_2/KB positive electrode shows much lower voltage polarization than that with S/KB at the examined rates (Supplementary Fig. 3b–d). All S_8I_2/KB cells were operated by starting with charging (instead of discharging) for the first cycle, the reason for which is discussed below. For comparison, the cell with mechanically milled Li_2S-LiI ($n(Li_2S)$: $n(LiI)$ = 8:2 mol/mol) as the active material was also assembled (see "**Methods**"). The cell exhibits a capacity of 620.0 mA h $g^{-1}_{S/I}$ when charged at 1 C (0.8 mA cm^{-2}) and maintains only 315.9 mA h $g^{-1}_{S/I}$ at 20 C (15.5 mA cm^{-2}) (Supplementary Fig. 4a, b). Therefore, the carbon-encapsulated nanometric homogenized S_8I_2/KB positive electrode enables improved fast-charging performance compared to pure sulfur or milled Li_2S-LiI composites. Increased polarization voltages are observed at higher charging rates for these cells; this is attributed to the elevated overpotential at the In/InLi counter electrode and the increased ohmic resistance at higher currents (discussed in Supplementary Fig. 4c, d). Furthermore, the S_8I_2/KB cell also shows good discharging rate capability, with 1033.3 mA h $g^{-1}_{S/I}$ and 892.3 mA h $g^{-1}_{S/I}$ when discharged at 3 C (2.8 mA cm^{-2}) and 5 C (4.7 mA cm^{-2}), respectively, indicating the enhanced ionic/electronic transport in the lithiated S_8I_2/KB positive electrode by LiI (Supplementary Fig. 5). The impact of the applied stack pressures on the rate capability is discussed in Supplementary Fig. 6. The cell with an S_8I_2/KB positive electrode using a pure lithium metal negative electrode at the low stacking pressure of 11 MPa exhibits very stable cycling in terms of both the capacity and voltage polarizations (Supplementary Fig. 7).

The S_8I_2/KB cells with $Li_7P_3S_{11}$ and Li_3PS_4 catholytes also show good fast-charging performance. The S_8I_2/KB cell with $Li_7P_3S_{11}$ catholyte exhibits a high capacity of 925.4 mA h $g^{-1}_{S/I}$ at a charging rate of 3 C (3.1 mA cm^{-2}), and maintains 725.4 mA h $g^{-1}_{S/I}$ at 10 C (10.4 mA cm^{-2}); the cell still shows a high capacity of 439.7 mA h $g^{-1}_{S/I}$ at 24 C (24.9 mA cm^{-2}) (Fig. 2f, g and Supplementary Fig. 3e). The S_8I_2/KB cell with Li_3PS_4 catholyte exhibits a capacity of 1036.2 mA h $g^{-1}_{S/I}$ at a

https://doi.org/10.1038/s41467-026-78042-6

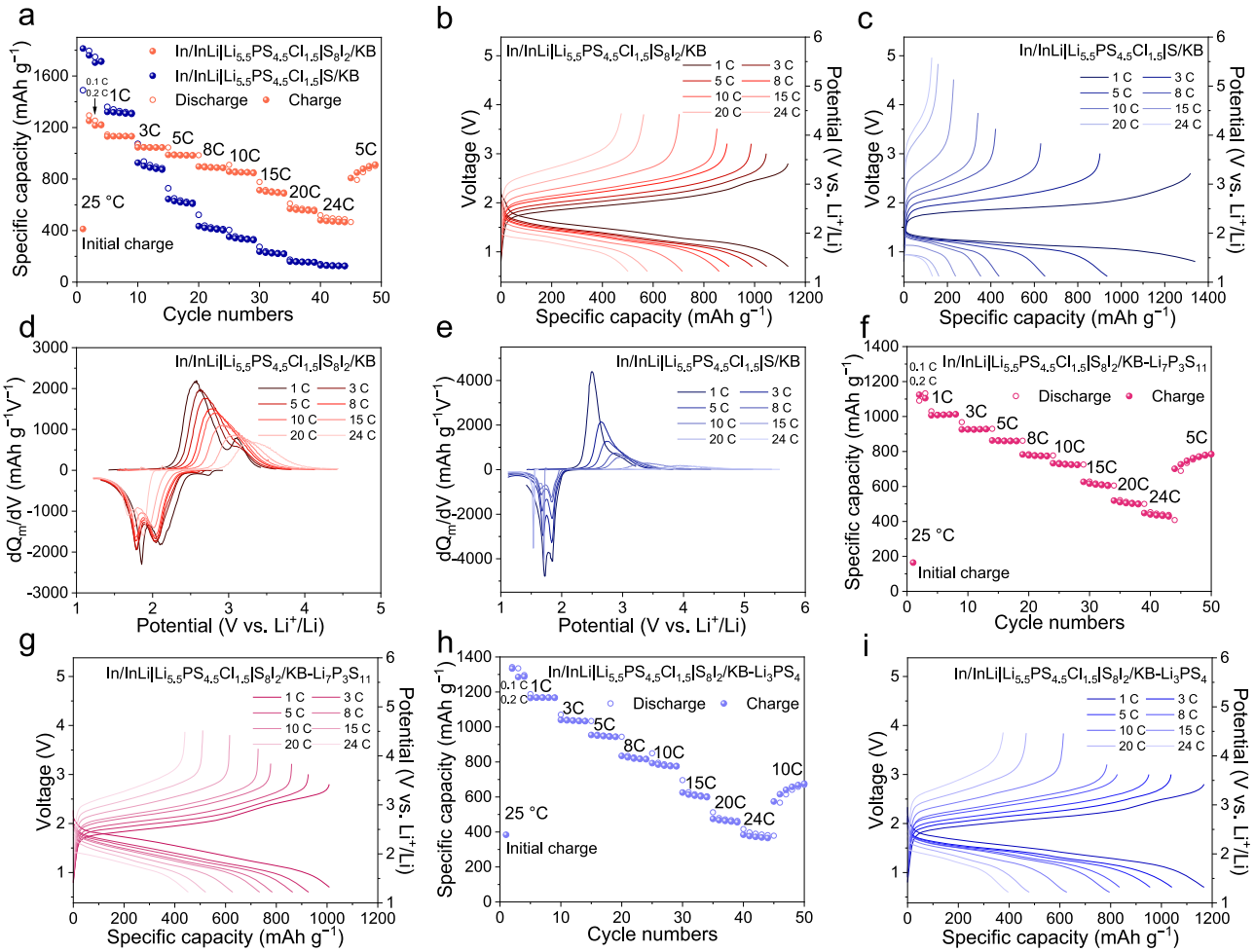


Fig. 2 | Fast-charging performance of S_8I_2/KB based all-solid-state lithium-sulfur batteries at 25 °C. a Charging rate capability of the cell using the amorphous S_8I_2/KB nanocomposite with $Li_{5.5}PS_{4.5}Cl_{1.5}$ catholyte at varied charging rates (labeled); the cell using the pure sulfur S/KB composite is shown for comparison. A constant discharging rate of 2 C is used for all S_8I_2/KB cells (**a**, **f**, **h**), and a constant discharging rate of 1 C is used for the S/KB cell (**a**). **b**, **c** Discharge-charge voltage profiles for the cells using S_8I_2/KB (**b**) and S/KB composites (**c**), respectively. **d**, **e** The corresponding differential capacity (dQ_m/dV) plots for the cells using S_8I_2/KB (**d**) and S/KB composites (**e**), respectively. **f**, **g** Charging rate capability of the cell using S_8I_2/KB with $Li_7P_3S_{11}$ catholyte (**f**), and the corresponding voltage profiles (**g**). **h**, **i** Charging rate capability of the cell using S_8I_2/KB with Li_3PS_4 catholyte (**h**), and the corresponding voltage profiles (**i**). Potentials are presented vs. Li^+/Li, assuming an In/InLi potential of 0.62 V vs. Li^+/Li. Cells were activated by cycling at 0.1 and 0.2 C prior to rate capability measurements. Cells using S_8I_2/KB are charged first and show an appreciable first-cycle charging capacity. The specific currents of 1 C are 1672 mA g^{-1}_S and 945 mA $g^{-1}_{S/I}$ for S/KB and S_8I_2/KB positive electrodes, respectively. The loadings of S_8I_2 in the S_8I_2/KB positive electrodes and S in the S/KB positive electrode are 1.1 and 1.0 mg cm^{-2}, respectively.

charging rate of 3 C (3.1 mA cm^{-2}), and maintains 779.0 mA h $g^{-1}_{S/I}$ and 376.6 mA h $g^{-1}_{S/I}$ at 10 C (10.4 mA cm^{-2}) and 24 C (24.9 mA cm^{-2}), respectively (Fig. 2h, i and Supplementary Fig. 3f). Therefore, the improved solid-solid sulfur redox reaction of the S_8I_2/KB positive electrode is not limited to a particular catholyte (e.g., Cl-containing SEs), but is effective in general with sulfide SEs. The fact that the three S_8I_2/KB positive electrodes exhibit similarly fast-charging performances despite the varied ionic conductivity of the three catholyte SEs (discussed in Supplementary Fig. 8) indicates that the catholyte SE conductivity is not limiting the kinetics of the solid-solid sulfur reaction. This adds strong evidence for a specific mechanism that occurs only in the iodine pre-embedded positive electrode.

The mechanism of fast solid-solid sulfur reaction

To understand the origin of the fast solid-solid sulfur reaction in the amorphous nano-eutectic S_8I_2/KB electrode, we first investigate the chemical state of the pristine S_8I_2/KB-$Li_{5.5}PS_{4.5}Cl_{1.5}$ composite. While the pristine S_8I_2/KB is amorphous, interestingly, upon milling of S_8I_2/KB with the $Li_{5.5}PS_{4.5}Cl_{1.5}$ catholyte, crystalline LiI forms as evidenced by XRD (Fig. 3a and Supplementary Fig. 9a). This indicates that a fraction of iodine in S_8I_2/KB reacts with $Li_{5.5}PS_{4.5}Cl_{1.5}$ to form LiI, as indicated in Eq. 1. To verify the reaction, we milled pure I_2 with $Li_{5.5}PS_{4.5}Cl_{1.5}$ and the product clearly shows the presence of LiI (Fig. 3a). The chemical state of iodine in S_8I_2/KB-$Li_{5.5}PS_{4.5}Cl_{1.5}$ is further explored by XANES. The I K-edge spectrum of the pristine S_8I_2/KB electrode exhibits a pre-edge/edge feature combined from the two references I_2/C and LiI/C, indicating the presence of both LiI and I_2 (Supplementary Fig. 9b). Further, as the S_8I_2 is spatially encapsulated within the mesopores of carbon, the reaction of Eq. 1 is expected to occur at the S_8I_2/KB particle surface that is in contact with the SE catholyte. In other words, we suggest that LiI is formed at the S_8I_2/KB | SE boundaries, such that a global distribution of LiI is generated through the electrode, that is, at the surface and in the pores of S_8I_2/KB particles (schematically shown in Fig. 3b). We also assume that this network is redox-active and converts between LiI and I_2 during cycling. The distribution of LiI is also indicated by high-resolution TEM imaging (Fig. 3c). The high-angle annular dark-field scanning transmission electron microscopy (HAADF-STEM) imaging and the EDX mapping show the distribution of I in the bulk and on the edge of the particle and its uniform presence with $Li_{5.5}PS_{4.5}Cl_{1.5}$ elements (Supplementary

https://doi.org/10.1038/s41467-026-78042-6

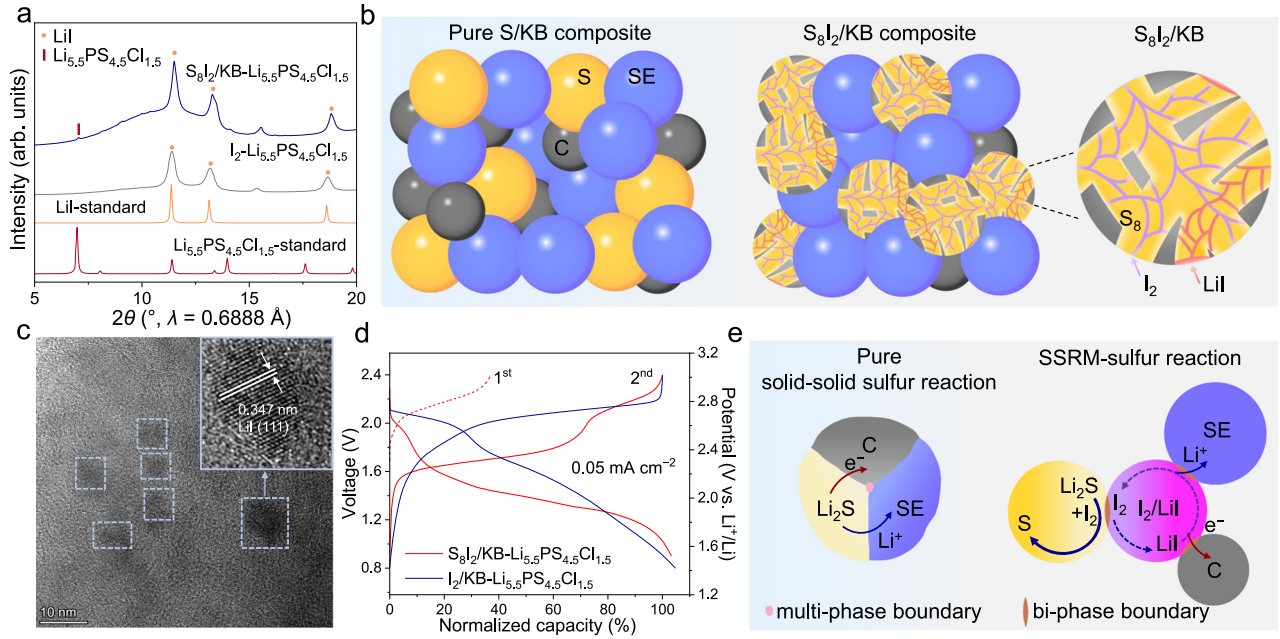


Fig. 3 | Microstructure and proposed solid-soild redox mediation (SSRM) mechanism for the S_8I_2/KB composite electrode. a Synchrotron X-ray diffraction patterns of the S_8I_2/KB-$Li_{5.5}PS_{4.5}Cl_{1.5}$ positive electrode (50 wt% of S_8I_2) and milled I_2-$Li_{5.5}PS_{4.5}Cl_{1.5}$ (37.5 wt%:62.5 wt%), with standard patterns of $Li_{5.5}PS_{4.5}Cl_{1.5}$ and LiI. **b** Schematic illustration of the pure S and the S_8I_2/KB composite; the inner pore and surface structure of S_8I_2/KB is presented as enlarged. **c** A representative transmission electron microscopy image of pristine S_8I_2/KB-$Li_{5.5}PS_{4.5}Cl_{1.5}$ composite with multiple distributed crystallites that are indexed to be LiI (111). **d** The charge-discharge voltage profiles of the S_8I_2/KB cell (current: 0.05 mA cm^{-2}, dashed line for the 1st charge) and the pure iodine I_2/KB-$Li_{5.5}PS_{4.5}Cl_{1.5}$ cell (current: 0.05 mA cm^{-2}). Potentials are presented vs. Li^+/Li, assuming an In/InLi potential of 0.62 V vs. Li^+/Li. **e** Schematic illustration of the SSRM mechanism for the fast-charging S_8I_2/KB positive electrode.

Fig. 9d). Note that the moderate ionic conductivity of LiI is also expected to enhance Li^+ ion transport within the composite (Supplementary Fig. 9c).

$$xI_2 + Li_{5.5}PS_{4.5}Cl_{1.5} \rightarrow 2xLiI + Li_{5.5-2x}PS_{4.5-x}Cl_{1.5} + xS \quad (1)$$

The redox reactions of sulfur and iodine in the S_8I_2/KB positive electrode upon cycling were then examined at low rates to reveal the close-to-equilibrium behavior. Starting by charging the cell at 0.05 mA cm^{-2}, the S_8I_2/KB positive electrode shows a considerable capacity of 468.3 mA h $g^{-1}_{S/I}$ with a well-defined plateau at ~ 2.8 V (vs. Li^+/Li) (Fig. 3d dashed line, Supplementary Fig. 10a, b). The cell further shows a plateau at ~ 2.6 V upon discharge and a ~ 2.8 V plateau on second charge – in addition to the redox plateau of sulfur – confirming the reversibility of the redox reactions (Fig. 3d). Further, when starting with discharging, the S_8I_2/KB positive electrode still shows the same redox behavior (Supplementary Fig. 10e, f). In contrast, the pure sulfur S/KB positive electrode does not show such redox behavior (Supplementary Fig. 10a, c). This points to an iodine-based redox reaction where a fraction of LiI in the S_8I_2/KB composite is oxidized (along with other SE decomposition reactions[39,53]) during the first cycle. Indeed, the iodine (I^-/I_2) reportedly shows a thermodynamic redox potential of 2.8 V[50,54]. In fact, we assembled cells using pure I_2 as the active material, and the cell shows highly reversible redox behavior at ~ 2.8/2.6 V (vs. Li^+/Li) (Fig. 3d and Supplementary Fig. 10d, g–i), which confirms that the iodine redox indeed can occur in the S_8I_2/KB positive electrode from a thermodynamic point of view. Further discussion on the redox behavior of the I^-/I_2 couple, confirmed by varying the catholytes, is referred to Supplementary Figs. 11, 12. Our analysis on the In/LiIn counter electrode surface after cycling further shows the absence of iodine shuttling to the negative electrode, ensuring long-term stability of iodine redox in the cells (Supplementary Fig. 13).

The redox potential of the I^-/I_2 couple (~ 2.8/2.6 V) is higher than that of Li_2S/S (~2.3 V); therefore, this difference offers enough thermodynamic driving force for I_2 to chemically oxidize xLi_2S/Li_2S_x in contact (Eq. 2), featuring a solid-solid redox-mediation mechanism (SSRM, schematically shown in Fig. 3e). The SSRM effect enabled by this pre-embedded redox mediator is amplified by the nanometric composite within the porous carbon and the global distribution of I_2/I^- in the S_8I_2/KB positive electrode. SSRM is particularly effective at high charging rates when the solid-solid sulfur reaction usually causes high overpotentials due to the limited number of reaction sites (multi-phase boundaries). Upon charge, the fast I_2/I^- reaction occurs first (bi-phase boundaries) and redox-mediates the sulfur reaction (bi-phase boundaries; Fig. 3e). Indeed, as shown by the voltage profiles (Fig. 2b), as opposed to the well-separated two plateaus of sulfur and iodine redox at low charging rates of 1C-3C (i.e., cascade reactions), at high charging rates the charging profiles show one integrated plateau. The PE-SSRM thus enables transformation from the sluggish, boundary-demanding solid-solid sulfur reaction to a boundary-cooperative sulfur reaction that is rapid, spatially homogeneous and reversible. The investigation of the SSRM effect is discussed in the following section.

$$I_2 + Li_2S \rightarrow 2LiI + S \quad (2)$$

Characterization of the SSRM effect

To confirm the chemical speciation during the iodine/sulfur redox in the S_8I_2/KB positive electrode, we examine the operando I K-edge and ex situ S K-edge XANES spectra of the positive electrode over charge/discharge (Fig. 4a–e). The spectra of standards of I_2/C, LiI/C, Li_2S/C, S/C and $Li_{5.5}PS_{4.5}Cl_{1.5}$ were measured for reference. The cell setup for operando XANES measurement is shown in Supplementary Fig. 14. The operando I K-edge XANES spectra reveal that, at the beginning of the initial charge (SOC: 0 – 44%), the pre-edge area (33170 – 33173 eV)

https://doi.org/10.1038/s41467-026-78042-6

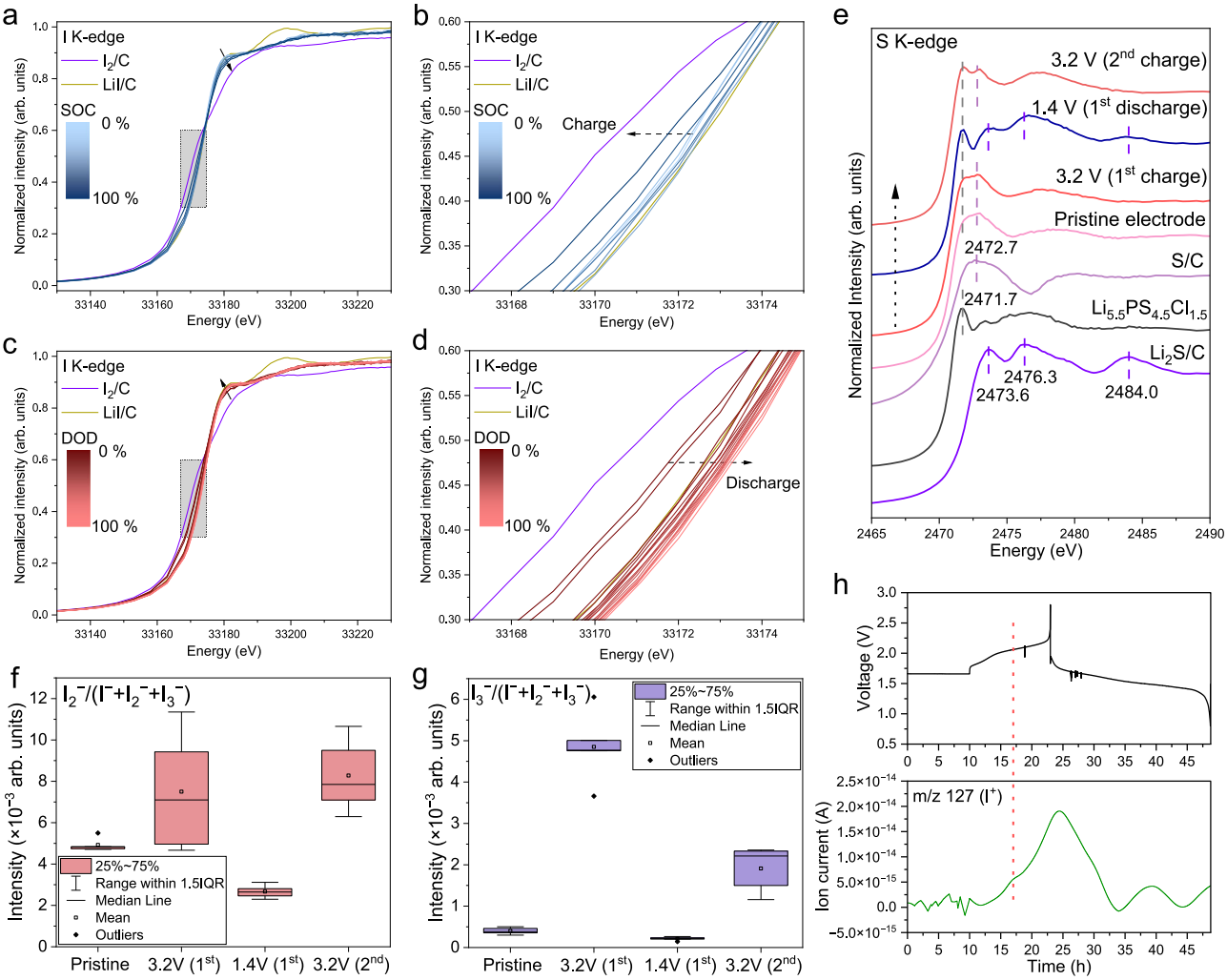


Fig. 4 | Mechanistic studies of the solid-solid redox mediation for S_8I_2/KB positive electrode. a–**d** Operando I K-edge X-ray absorption near edge structure (XANES) spectra studies: (**a**, **b**) Operando evolution of the I K-edge XANES spectra during the first charge (**a**), along with the magnified view (**b**). **c**, **d** Operando evolution of the I K-edge XANES spectra during the following discharge (**c**), along with the magnified view (**d**). The cell was measured at 0.19 mA cm^{-2} (0.2 C) at 25 °C. The spectra of I_2/C and LiI/C are shown as references. **e** Ex situ S K-edge XANES spectra of the positive electrode in pristine state, after first charge to 3.2 V, after subsequent discharge to 1.4 V, and after the second charge to 3.2 V vs Li^+/Li; Li_2S/C, S/C and $Li_{5.5}PS_{4.5}Cl_{1.5}$ were measured as references. The feature at 2471.7 eV corresponds to $Li_{5.5}PS_{4.5}Cl_{1.5}$. **f**, **g** Surface analysis of the I_2^- (**f**) and I_3^- (**g**) fragments for the S_8I_2 positive electrode at different states (pristine, first charge to 3.2 V, discharge to 1.4 V, and second charge to 3.2 V vs Li^+/Li) by time-of-flight secondary-ion mass spectrometry (TOF-SIMS). The box plots were obtained from five different spots on the same sample ($n = 5$). IQR, interquartile range. The catholyte SE used for these cells is $Li_{5.5}PS_{4.5}Cl_{1.5}$. For ex situ characterization, cells were cycled at 0.05 C and 25 °C before disassembly. Samples were collected at the stage of first charge to 100% SOC (3.2 V), first discharge to 100% DOD (1.4 V), and second charge to 100% SOC (3.2 V). **h** In situ gas analysis of a cell with the configuration In/InLi|LPSCl|S_8I_2/KB-$Li_{5.5}PS_{4.5}Cl_{1.5}$ at 45 °C by differential electrochemical mass spectrometry (DEMS).

shows marginal variations (closer to that of LiI). This confirms the absence of iodine redox at a potential of < 2.7 V (vs. Li^+/Li). Once the cell reaches the potential of 2.7 V (SOC: 44 – 100%), the I K-edge shows a noticeable shift toward that of I_2, indicating the occurrence of an oxidation process from I^- to I_2 within the positive electrode (Fig. 4a, b). This confirms the oxidation of LiI in the cell at the potential of 2.7 V – 2.8 V vs. Li^+/Li. The cell was then discharged to examine the reduction of iodine. At the beginning of discharge (Fig. 4c, d), the I K-edge shifts to higher energy toward LiI, indicating reduction of iodine from I_2 to I^- around the potential of 2.5 V vs. Li^+/Li. As the discharge continues (< 2.2 V vs. Li^+/Li), the I K-edge remains largely unchanged and maintains the LiI-like state throughout the subsequent discharge, consistent with the absence of iodine reduction in this potential range. Therefore, the operando XANES measurement provides evidence of the behavior of I^-/I_2 redox in the S_8I_2/KB positive electrode. Ex situ S K-edge XANES spectra collected upon the initial charge to 3.2 V show two unchanged characteristic peaks at 2471.7 and 2472.7 eV, which are assigned to sulfur species in $Li_{5.5}PS_{4.5}Cl_{1.5}$ and the S^0 active material, respectively (Fig. 4e). The subsequent discharge to 1.4 V leads to the full conversion of S into Li_2S (with post-edge features at 2473.6, 2476.3, and 2484.0 eV), as well as the appearance of S upon second charge, confirming the reversible S/Li_2S conversion (Fig. 4e).

With the confirmed occurrence of reversible iodine/sulfur redox in the S_8I_2/KB composite, we further examined the oxidized iodine species via time-of-flight secondary-ion mass spectrometry (TOF-SIMS). Upon initial charge to 3.2 V, we observe a statistically significant increase of I_2^- (and I_3^-) species, as quantified by the intensity of the I_2^- (and I_3^-) signals normalized to the sum of I^-, I_2^- and I_3^- (Fig. 4f, g). This suggests that the oxidation products are I_2 (along with a small fraction of I_3^-). The formation of I_3^- can be attributed to the combination reaction of I_2 with I^- at equilibrium. Beyond discharge to 1.4 V, the amount of I_2^- and I_3^- species decreases and is lower than in the pristine

positive electrode, indicating that the I_2 in the pristine positive electrode was partially activated to undergo redox mediation and was reduced to I^- on discharge. The amount of I_2^- and I_3^- species increases again after the following charge, confirming a reversible behavior. The 3D profiling of I^- and I_2^- for the S_8I_2/KB positive electrode shows a uniform distribution over a 50 × 50 μm² area, and the evolution of I^- and I_2^- distribution consistently confirms that I_2 is formed upon charge and that I^- is formed on discharge, confirming the reversible redox behavior of I^-/I_2 (Supplementary Figs. 15a, b). In situ differential electrochemical mass spectrometry (DEMS) analysis was further performed to confirm the formation of I_2 upon charge of the cell. As shown in Fig. 4h, a clear surge of the signal with $m/z = 127$ starts (~ 17 h) at about 2.1 V vs. In/InLi (i.e., ~ 2.7 V vs. Li^+/Li), which continues to surge over the rest of the charge (and peaks shortly after the onset of charge). This signal at $m/z = 127$ is attributed to I^+, which herein is a fragment from the ionization of I_2 (further discussions in "**Methods**").

The question that remains is whether the I^-/I_2 redox can indeed chemically mediate the solid-solid Li_2S oxidation in the cell. To support our hypothesis on the function of SSRM, we mixed an equimolar ratio of Li_2S and I_2 through gentle 20 min ball-milling at 80 rpm or by a simple 2 min hand grinding, mimicking the proposed solid-state redox mediation reaction (Eq. 2)[44,55,56]. We clearly observe the formation of LiI and S in the product by XRD and Raman spectroscopy (Supplementary Figs. 15c, d), validating a rather fast chemical reaction. This indicates that the SSRM effect by pre-embedded I_2/LiI redox mediators indeed occurs in the S_8I_2/KB cell. This is further supported by in situ EIS measurement of the S_8I_2/KB cell wherein a new semicircle at medium frequencies appears when charged to 2.8 V, indicating the formation of a new interface ascribed to the oxidation of LiI to I_2 (Supplementary Fig. 16).

By pre-embedding the iodine redox mediator via encapsulation in carbon mesopores and homogenizing it with the sulfur active material on the nanoscale, the eutectic S_8I_2/KB positive electrode provides good fast-charging capability through the SSRM effect. The mechanism in the S_8I_2/KB nanocomposite is distinct from the reported $S_{9.3}I$ compound[32]. Different from the increased electronic conductivity owing to molecular insertion of I into S_8 ring, which improves the sulfur reaction kinetics (of physical origin), our approach relies on the chemical interplay between the sulfur redox and iodine redox, which essentially offers short cuts for charge transfer from the SE and carbon to the solid Li_2S/Li_2S_x (of chemical origin). Furthermore, we show that the PE-SSRM effect also extends to the $S_{9.3}I$/KB composite prepared with carbon encapsulation (Supplementary Fig. 17).

The SSRM reported here is further distinguished from the redox mediation in liquid electrolytes, wherein the redox mediators are dissolved in the electrolytes and mediate the reactions at the liquid-solid interfaces (the discharge products of Li_2S/Li_2O_2 have limited access *only* to electrons due to their large particle sizes)[55,56]. In contrast, for ASSLSBs, the oxidation of Li_2S is kinetically limited by its access to both electrons and Li^+, due to the low population of Li_2S|carbon|SE multiphase boundaries. Therefore, not only chemical aspects (redox potential difference, ionic conductivity, intrinsic reaction kinetics), but also structural aspects of the redox mediator (nanometric homogenization with sulfur) must be considered. The ability of iodine to form a eutectic solution with sulfur (associated with the high miscibility of the two phases) enables such structural manipulation. Importantly, the iodine exhibits high vapor pressure and may readily diffuse in its atomic form along the porous surface of carbon and voids within the positive electrode (further discussed in Supplementary Figs. 18, 19), thereby enabling rapid contact with the adjacent Li_2S and facilitating its oxidation (Fig. 3e). The importance of nanometric homogenization is showcased through experiments on S_8I_2 positive electrodes prepared from low-surface-area carbon (Supplementary Fig. 20).

Long-term stability of the ASSLSBs

The long-term cycling stability of the cells with the eutectic S_8I_2/KB positive electrode was examined using sulfide SEs and In/LiIn counter electrodes. The cell with S_8I_2/KB and Li_3PS_4 catholyte shows a high specific capacity of 1219.4 mA h $g^{-1}_{S/I}$ and retains 81.4 % capacity over 2,800 cycles at 0.5 C (0.49 mA cm^{-2}) (Fig. 5a and Supplementary Fig. 21a). The cell has operated steadily for over 17 months. This proves the high reversibility of the redox-mediated reaction in S_8I_2/KB and the good solid-solid mechanical contact, which greatly reduces the formation of isolated Li_2S or S during cycling. We believe the suppressed chemo-mechanical degradation is partially attributed to the formation of a globally distributed I_2/I^- nano-network through the positive electrode by reaction of iodine with the sulfide SE-catholyte in situ, which is beneficial for maintaining interfacial contact and mediation during prolonged cycling.

The cells also demonstrate good long-term cycling stability at high rates. At a charge/discharge rate of 5 C (5.3 mA cm^{-2}), the S_8I_2/KB cell with $Li_{5.5}PS_{4.5}Cl_{1.5}$ catholyte shows an initial capacity of 898.8 mA h $g^{-1}_{S/I}$ and maintains 92.0 % capacity after 3,400 cycles with highly stable voltage profiles (Fig. 5b, d). The origin of the polarization at high current densities is discussed in Supplementary Fig. 22. Furthermore, even at a high charging rate of 10 C (12.7 mA cm^{-2}; here discharged at 2 C), the cell can show a capacity of 650.3 mA h $g^{-1}_{S/I}$ and maintains 80.6 % of its capacity after 5000 cycles (Fig. 5c, e). The long-term stability and high-rate performance of S_8I_2/KB positive electrode are competitive with previously reported ASSLSBs with sulfur or Li_2S-based positive electrodes (Supplementary Table S1). It should be noted that direct comparisons among different studies should be made with caution, as the reported performance can be influenced by variations in experimental conditions.

Further, we demonstrate long-term stability for cells with electrodes with higher S_8I_2 loading. The S_8I_2/KB cell loaded with 3.0 mg cm^{-2} exhibits a capacity of 943.9 mA h $g^{-1}_{S/I}$ (2.8 mA h cm^{-2}), and it retains 83.7 % capacity after 1500 cycles at a 1 C charge/discharge rate (2.8 mA cm^{-2}) (Supplementary Fig. 21b, c). With a high S_8I_2 loading of 5.0 mg cm^{-2}, the cell still shows a high capacity of 771.9 mA h $g^{-1}_{S/I}$ (3.9 mA h cm^{-2}) and retains 80.3 % after 1,600 cycles at a 1 C charge/discharge rate (4.7 mA cm^{-2}) (Fig. 6aand Supplementary Fig. 21**d**). Furthermore, with an even higher S_8I_2 loading of 10.0 mg cm^{-2}, the cell displays a high capacity of 1023.3 mA h $g^{-1}_{S/I}$ (10.2 mA h cm^{-2}) at 0.47 mA cm^{-2} and 931.4 mA h $g^{-1}_{S/I}$ (9.3 mA h cm^{-2}) at 0.94 mA cm^{-2} (0.1 C) with 87.9 % capacity retention over 100 cycles (Fig. 6b and Supplementary Fig. 21e). The demonstrated cycling performance with high areal capacity and long-term stability is competitive with that of ASSLSBs and even LMO-based ASSLBs (Supplementary Table S1).

We further increased the fraction of S_8I_2 to 50 wt% on the electrode level (with 30 wt% $Li_{5.5}PS_{4.5}Cl_{1.5}$ and 20 wt% carbon), and observed that the cell shows an initial capacity of 786.3 mA h $g^{-1}_{S/I}$ at 2 C (2.4 mA cm^{-2}) and retains 75.8 % capacity after 9000 cycles (S_8I_2 loading:1.3 mg cm^{-2}, Fig. 6c, d). With an S_8I_2 loading of 4.9 mg cm^{-2}, the cell achieves a high capacity of 702.8 mA h $g^{-1}_{S/I}$ (3.4 mA h cm^{-2}) and retains 80.7 % capacity after 300 cycles at 0.1 C (0.46 mA cm^{-2}) (Supplementary Fig. 23a, b). To further demonstrate the concept at higher fractions of active material in the positive electrode, we prepared positive electrodes with a high electrode-level S_8I_2 fraction of 60 wt% (21 wt% $Li_{5.5}PS_{4.5}Cl_{1.5}$ and 19 wt% carbon). The cell loaded with 1.1 mg cm^{-2} of S_8I_2 shows a specific capacity of 852.5 mA h $g^{-1}_{S/I}$ at 1 C (1.1 mA cm^{-2}) and retains 86.1% capacity after 500 cycles (Supplementary Fig. 23c, d). The cell with a high loading of 3.4 mg cm^{-2} delivers a specific capacity of 900.3 mA h $g^{-1}_{S/I}$ at 0.16 mA cm^{-2} (0.05 C) and shows stable cycling, retaining 722.4 mA h $g^{-1}_{S/I}$ after 200 cycles at 0.2 C (Fig. 6e and Supplementary Fig. 24a).

We further examined the cells with both high fraction and high areal loadings of S_8I_2. The cell with 50 wt% and 9.8 mg cm^{-2} of S_8I_2 exhibits a high areal capacity of 8.5 mA h cm^{-2} (865.6 mA h $g^{-1}_{S/I}$) at a

https://doi.org/10.1038/s41467-026-78042-6

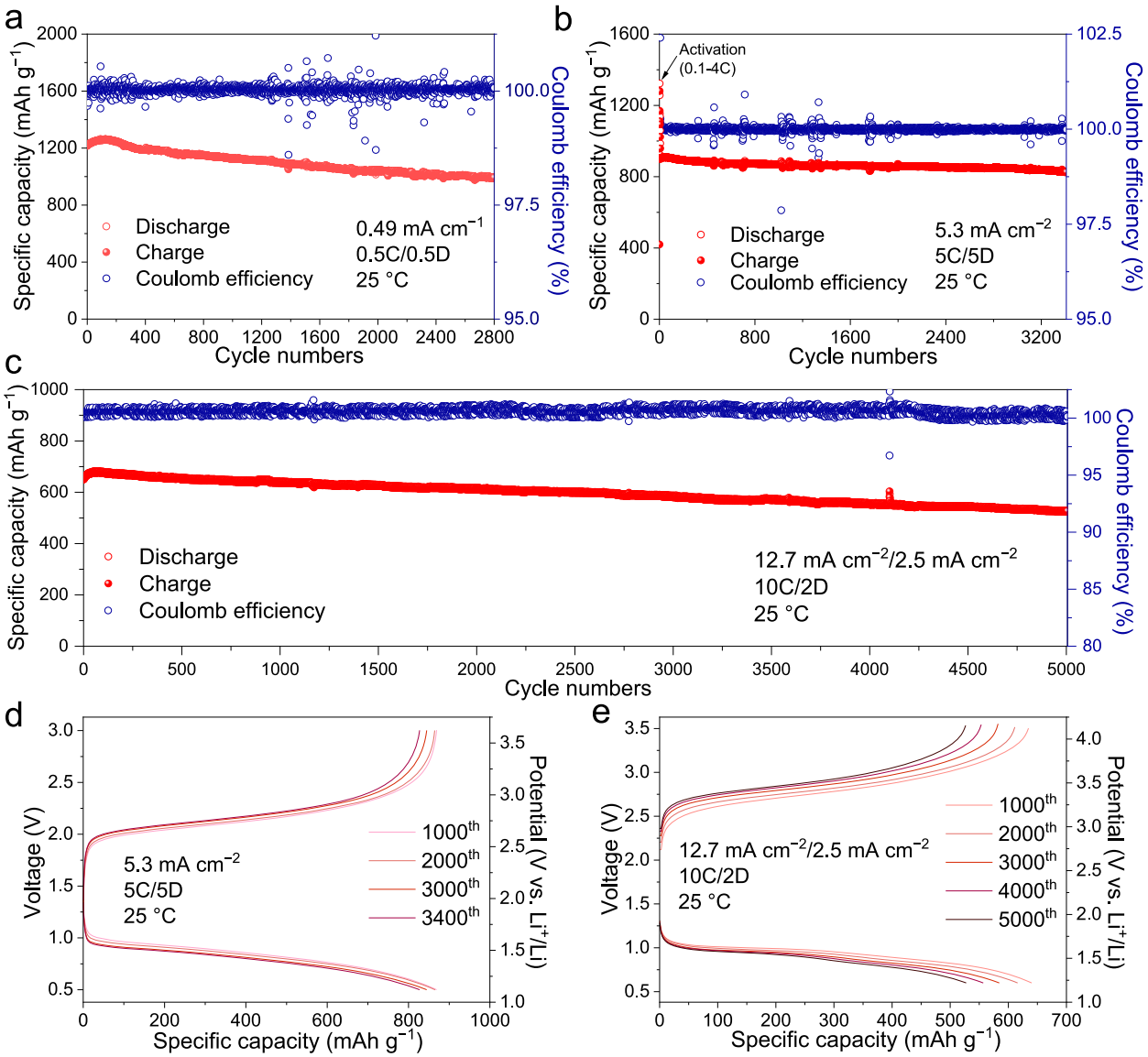


Fig. 5 | Long-term cycling performance of S_8I_2/KB based all-solid-state lithium-sulfur batteries at 25 °C. a Long-term cycling of the S_8I_2/KB cell with Li_3PS_4 catholyte at a 0.5 C rate (0.49 mA cm^{-2}, S_8I_2 loading: 1.0 mg cm^{-2}). **b** Long-term cycling of the S_8I_2/KB cell with $Li_{5.5}PS_{4.5}Cl_{1.5}$ catholyte at a 5 C (discharging/charging) rate (5.3 mA cm^{-2}, S_8I_2 loading: 1.1 mg cm^{-2}); the cell was activated by cycling at rates ranging from 0.1 to 4 C for the first seven cycles. **c** Long-term cycling of the S_8I_2/KB cell with $Li_{5.5}PS_{4.5}Cl_{1.5}$ catholyte at a charging/discharging rate of 10 C/2 C (12.7 mA cm^{-2}/2.5 mA cm^{-2}, S_8I_2 loading: 1.3 mg cm^{-2}). **d**, **e** Discharge–charge voltage profiles of the cells at 5 C (**d**) and 10 C (**e**) rates, respectively. 1 C = 945 mA g$^{-1}_{S/I}$. Potentials are presented vs. Li$^+$/Li, assuming an In/InLi potential of 0.62 V vs. Li$^+$/Li. Cells were tested in a custom pressure cell configuration.

current density of 0.46 mA cm^{-2} and sustains 35 cycles with 80.8% capacity retention (Supplementary Fig. 24b, c). Further, the cell with electrode-level 60 wt% and 7.7 mg cm^{-2} of S_8I_2 displays a specific capacity of 547.1 mA h g$^{-1}_{S/I}$ at a current density of 0.36 mA cm^{-2}, and retains 562.8 mA h g$^{-1}_{S/I}$ over 50 cycles (Supplementary Fig. 24d, e). Additionally, the cell with an even higher loading of 9.7 mg cm^{-2} (electrode-level 60 wt% S_8I_2) shows stable operation for 100 cycles with a reversible capacity up to 750 mA h g$^{-1}_{S/I}$ at a current density of 0.28 mA cm^{-2} (Supplementary Fig. 25a, b). The cell with a very high electrode-level loading of 70 wt% (rest being 21 wt% solid electrolyte and 9 wt% carbon) still shows a gradually stabilized specific capacity of 601.5 mA h g$^{-1}_{S/I}$ with marginal capacity fade and highly reproducible profiles for 800 cycles (Supplementary Fig. 25c, d).

To demonstrate the PE-SSRM concept in a practical full cell setup, we developed S_8I_2/KB cells with a Li-Al negative electrode[17], and the cells show good rate performance. The S_8I_2/KB cell exhibits a high capacity of 1010.7 mA h g$^{-1}_{S/I}$ at a charging rate of 3 C (4.0 mA cm^{-2}), maintaining 797.0 mA h g$^{-1}_{S/I}$ and 544.4 mA h g$^{-1}_{S/I}$ at a charging rate of 10 C (13.5 mA cm^{-2}) and 18 C (24.2 mA cm^{-2}), respectively (Supplementary Fig. 26a, c, d). At a 10 C charging rate (13.5 mA cm^{-2}), the cell shows stable cycling over 300 cycles (Supplementary Fig. 26b). These results demonstrate the potential for practical high-energy ASSLSBs. Nevertheless, further efforts are required to address key challenges toward their practical application, including high-energy-density negative electrodes, lithium metal/electrolyte interfacial stability, and high-conductivity solid electrolytes[6,11,33,35,36,40,57]. Further information on the projected cell-level specific energy and specific power based on the demonstrated electrochemical parameters is provided in Supplementary Tables S2 and S3, with comparison to ASSLSBs and LMO-based solid-state batteries.

https://doi.org/10.1038/s41467-026-78042-6

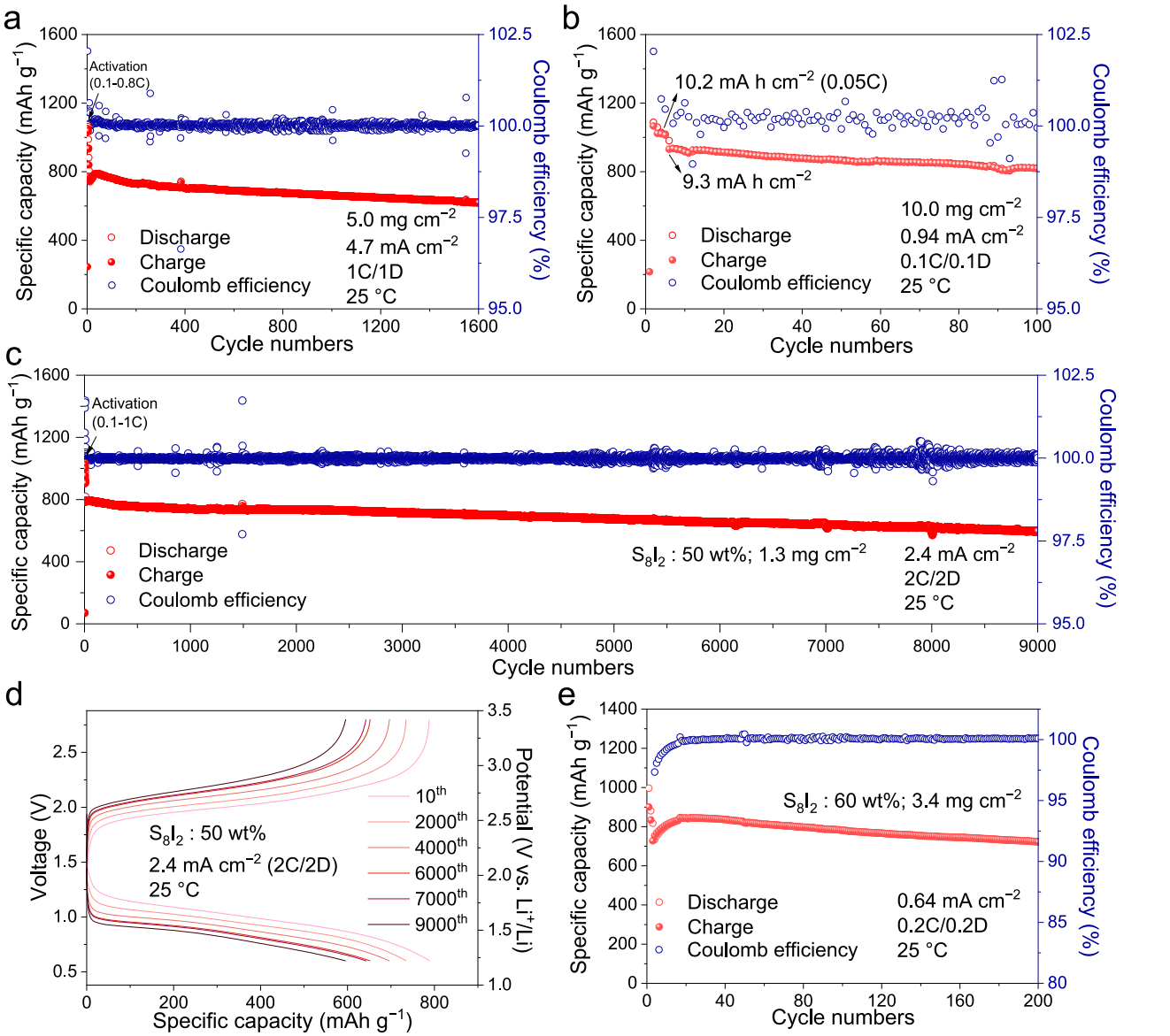


Fig. 6 | Long-term cycling performance of high-loading all-solid-state lithium-sulfur batteries with S_8I_2/KB-$Li_{5.5}PS_{4.5}Cl_{1.5}$ positive electrodes at 25 °C. a Long-term cycling of the cell at 1 C (4.7 mA cm^{-2}) with an S_8I_2 loading of 5.0 mg cm^{-2}; the cell was activated by cycling at rates ranging from 0.1 to 0.8 C for the first seven cycles. **b** Cycling performance of the cell with a high S_8I_2 loading of 10.0 mg cm^{-2} (30 wt% S_8I_2) at 0.1 C (0.94 mA cm^{-2}); the cell was activated at 0.03 C for 2 cycles and 0.05 C for 3 cycles. **c**, **d** Long-term cycling of the cell with a high S_8I_2 fraction of 50 wt% at 2 C (2.4 mA cm^{-2}) (**c**) and the corresponding discharge–charge voltage profiles (**d**) (S_8I_2 loading: 1.3 mg cm^{-2}); the cell was activated by cycling at rates ranging from 0.1 to 1 C for the first six cycles. **e** Long-term cycling of the S_8I_2/KB cell with 60 wt% S_8I_2 and S_8I_2 loading of 3.4 mg cm^{-2} at 0.2 C. The cell was activated at 0.05 C and 0.1 C for the first two cycles. 1 C = 945 mA g$^{-1}_{S/I}$. Potentials are presented vs. Li$^+$/Li, assuming an In/InLi potential of 0.62 V vs. Li$^+$/Li. Cells were tested in a custom pressure cell configuration.

Discussion

To summarize, in order to resolve the challenges associated with the slow solid-solid sulfur redox reactions, we describe a solid-solid redox mediation strategy using an amorphous sulfur/iodine nanocomposite positive electrode. The pre-embedded solid-solid redox mediators enable high-rate and long-life ASSLSBs. The nanometer-scale sulfur/iodine mixing in carbon mesopores lays the foundation for a strong SSRM effect by maximizing the number (density) of reactive mediation sites. Further, the iodine within and on the surface of carbon was found to spontaneously react with the sulfide SE-catholyte to form a percolated I_2/I^- nano-network through the positive electrode composite. The pre-embedded iodine distributed homogeneously on the nanoscale undergoes a rapid redox reaction in the form of I_2/I^-, which mediates the solid-solid sulfur reactions by promoting electron transfer across the solid-solid boundaries. Further elucidation of iodine transport within the electrode and its reaction kinetics with Li_2S and lithium polysulfides will be important for establishing a quantitative understanding of the dynamic iodine-mediated sulfur redox processes. Our PE-SSRM strategy offers an easily adoptable concept for developing all-solid-state conversion-based electrodes that are notoriously challenging due to poor reaction kinetics otherwise.

Methods

Synthesis of S_8I_2, S_8I_2/KB, S/KB and I_2/KB

The composite with the stoichiometry of S_8I_2 was synthesized by heating stoichiometric amounts of S (Alfa Aesar, 99%) and I_2 (Aladdin, 99.9%). Specifically, the S/I_2 mixture was pelletized and positioned inside a quartz tube, which was sealed under vacuum and heated at

80 °C for 10 h followed by natural cooling. To prepare the S_8I_2/KB, the S_8I_2 and Ketjenblack® (KB, EC-600JD, AkzoNobel, 99.9%) were mixed (75:25 or 8:2 or 9:1, wt/wt) by grinding and then heated at 100 °C inside a sealed quartz tube for 12 h to obtain the S_8I_2/KB composite. The S/KB (75:25, wt/wt) and I_2/KB (75:25, wt/wt) composites were obtained through heating, respectively, pure S and I_2 with KB inside a sealed quartz tube at 155 °C for 12 h.

Synthesis of solid electrolytes

$Li_{5.5}PS_{4.5}Cl_{1.5}$ was synthesized by ball milling and a subsequent annealing process. Stoichiometric amounts of LiCl (Alfa Aesar, 99%), P_2S_5 (Innochem, 99%), and Li_2S (Alfa Aesar, 99.9%) were ball-milled in a planetary ball mill (MSK-SFM-1, MTI) using a 50 mL zirconia jar and 5 mm-diameter zirconia balls. Unless otherwise specified, all ball-milling procedures described in "**Methods**" were carried out using the same model of ball mill, milling jar, and milling balls. The total mass of the zirconia balls was 20 g, corresponding to a ball-to-powder weight ratio of 20:1. Ball milling was performed at 500 rpm for 10 h, with a 5 min pause every 20 min and alternating rotation directions. The ball-milled material was pelletized and sintered at 500 °C for 15 h in a sealed quartz tube. The Li_3PS_4 and $Li_7P_3S_{11}$ electrolytes were synthesized through ball milling stoichiometric amounts of P_2S_5 and Li_2S. The ball milling procedure was the same as that of ball milling $Li_{5.5}PS_{4.5}Cl_{1.5}$, except that the milling time was extended to 38 h; no heat treatment was performed on these two solid electrolytes to maintain amorphous states. All electrolytes were ground prior to use. The operation was carried out in an argon-filled glovebox (H_2O < 0.1 ppm, O_2 < 0.1 ppm).

Chemical reaction between Li_2S and I_2

To validate the redox mediation of the Li_2S reaction by I_2, we performed the chemical reaction of Li_2S and I_2. Mixing of Li_2S and I_2 with a molar ratio of 1:1 by simple 2 min hand grinding was performed to prove the reaction. The product was then subjected to XRD and Raman measurements. In addition, stoichiometric amounts of Li_2S and I_2 with a molar ratio of 1:1 were ball-milled at 80 rpm for 20 minutes without intermittent rest periods. The total mass of the zirconia balls was 4 g, corresponding to a zirconia ball/material weight ratio of 20:1. The product was subjected to XRD and Raman spectroscopy measurements. The operation was carried out in an argon-filled glovebox (H_2O < 0.1 ppm, O_2 < 0.1 ppm).

Synthesis of positive electrode materials, cell assembly and cycling measurement

The S_8I_2/KB positive electrode composites loaded with 30 wt % of S_8I_2 were prepared by ball milling the S_8I_2/KB (75 wt% S_8I_2), Super P carbon (Timcal, 99.99%), and solid electrolyte ($Li_{5.5}PS_{4.5}Cl_{1.5}$, Li_3PS_4 or $Li_7P_3S_{11}$) with a weight ratio of 4: 1: 5 at 500 rpm for 20 hours. Unless otherwise specified, all ball-milling experiments in this section were conducted with a 5 min pause every 20 min and alternating rotation directions. The total mass of the zirconia balls was fixed at 16 g, corresponding to a ball-to-powder weight ratio of 40:1. The S_8I_2/KB positive electrode composites loaded with 50 wt % of S_8I_2 were prepared by ball milling the S_8I_2/KB (75 wt% S_8I_2), Super P, and $Li_{5.5}PS_{4.5}Cl_{1.5}$ with a weight ratio of 6.667: 0.503: 2.83 at 500 rpm for 20 h. The S_8I_2/KB positive electrode composites loaded with 60 wt % S_8I_2 were prepared by ball milling the S_8I_2/KB (80 wt% S_8I_2), Super P, and $Li_{5.5}PS_{4.5}Cl_{1.5}$ with a weight ratio of 7.5: 0.4: 2.1 at 500 rpm for 20 h. The S_8I_2/KB positive electrode composites loaded with 70 wt % S_8I_2 were prepared by ball milling the S_8I_2/KB (90 wt% S_8I_2), Super P, and $Li_{5.5}PS_{4.5}Cl_{1.5}$ with a weight ratio of 7.778: 0.122: 2.1 at 500 rpm for 20 h. For assembling the cells, 80 mg solid electrolyte powder (~ 0.5 mm thick) was placed into a polyetheretherketone (PEEK) cylinder (10 mm diameter; surface area: 0.785 cm^2) and pressed at 125 MPa for 1 min as the separator layer, and then the positive electrode composite was evenly spread on one side of the separator and pressed under 312 MPa for 3 min. On the other side of the separator, a thin indium foil (9 mm diameter, ~ 0.2 mm thick, 99.99%, Hefei Wenghe Metal Materials Co., Ltd) was attached, and a thin Li foil (7 mm diameter, ~ 0.1 mm thick, 99.9%, China Energy Lithium Co., Ltd.) was placed over the indium foil. Then, a pressure of 125 MPa was applied and maintained for 1 min. The assembly for cells with the S/KB and I_2/KB positive electrode remains the same, wherein the S/KB positive electrodes were made by ball milling S/KB composite, Super P, and $Li_{5.5}PS_{4.5}Cl_{1.5}$ with a weight ratio of 4: 1: 5 (S loading of 30 wt%) at 500 rpm for 20 h, and the I_2/KB positive electrodes were made by ball milling I_2/KB composite, Super P, and $Li_{5.5}PS_{4.5}Cl_{1.5}$ with a weight ratio of 4: 1: 5 (I_2 loading of 30 wt%) at 500 rpm for 20 h. For preparation of the Li_2S-LiI positive electrode, Li_2S:LiI (Alfa Aesar, 99.9%) with a molar ratio of 8:2 was pre-ball milled at 500 rpm for 10 h. Then, the milled Li_2S-LiI was ball milled with Super P with a weight ratio of 3:2 at 500 rpm for 10 h. After that, milled Li_2S-LiI-Super P was ball milled with $Li_{5.5}PS_{4.5}Cl_{1.5}$ with a weight ratio of 1:1 (Li_2S-LiI loading of 30 wt%) at 500 rpm for 12 h. The assembly procedure for cells with the Li_2S-LiI positive electrode remains the same as that for S_8I_2/KB cells. The assembly procedure for cells with Li-Al negative electrode remains the same as above, except that Al foil (9 mm diameter, 0.1 mm thick, 99.99%, Alfa Aesar) was used in place of In foil[17]. The mass considered in the described specific current (mA g^{-1}) and specific capacity (mA h g^{-1}) values refers to the mass of the active material in the electrode (S_8I_2, noted as S/I; or S). The $Li_{5.5}PS_{4.5}Cl_{1.5}$ was used as the separator electrolyte to evaluate the rate capability of these positive electrodes (S_8I_2/KB, S/KB and Li_2S-LiI) and of the cells with Li-Al negative electrode. The cells were assembled in an argon-filled glovebox (H_2O < 0.1 ppm, O_2 < 0.1 ppm). The Li_3PS_4 (low conductivity but stable with In/InLi) was used as the separator electrolyte for the long-term cycling of the S_8I_2/KB cell at 0.5 C. An iodine-doped sulfide SE synthesized by melt-quenching of Li_2S, LiI (Alfa Aesar, 99.9%), B_2S_3 (Macklin, 99.99%) and P_2S_5 (molar ratio of 3:4.5:2.5:0.5) at 800 °C was used as the separator electrolyte to evaluate the high-loading (3.0 ~ 10.0 mg cm^{-2}), high S_8I_2 wt% (50-70) and high-rate (≥ 2 C) long-term cycling cells in order to better stabilize the In/InLi counter electrode[48]. Cells were placed into a custom stainless-steel casing with an applied pressure of ~ 64 MPa. The SE-C electrodes of $Li_{5.5}PS_{4.5}Cl_{1.5}$-C, Li_3PS_4-C, Li_3PS_4·0.5LiI-C and $3Li_2S$-$2.5B_2S_3$-4.5LiI-C were obtained through ball milling these SEs and Super P with a weight ratio of 8: 2 at 500 rpm for 20 h. The Li_3PS_4·0.5LiI SE was obtained through the ball milling method, and the $3Li_2S$-$2.5B_2S_3$-4.5LiI SE was obtained through the melt-quenching method. The assembly of these cells using SE-C positive electrodes remains the same as that for the sulfur cells described above. The pressure applied to the cell with a Li-metal negative electrode was 11 MPa. The negative-to-positive capacity ratio was ~ 4:1 for positive-electrode active-material loadings ≤ 5 mg cm^{-2} and ~ 2:1 for loadings > 5 mg cm^{-2}. For preparation of the In/InLi symmetric cell, ~ 120 mg of $Li_{5.5}PS_{4.5}Cl_{1.5}$ powder was placed into the PEEK cylinder and pressed at 125 MPa for 1 min, then a thin indium foil and a thin Li foil were attached to each side of the electrolyte. The symmetric cells were placed into a custom stainless-steel casing with an applied pressure of ~ 30 MPa. Cells were placed in the temperature-controlled oven at 25 ± 1 °C for electrochemical cycling, unless otherwise specified. Galvanostatic cycling of the cells was performed using a Neware CT-4008Tn test system.

Physicochemical characterizations

The X-ray diffraction (XRD) analyses of synthesized materials were performed using a Rigaku MiniFlex600 X-ray diffractometer with Cu K_α radiation. To prevent air exposure, the powder samples were loaded into the sample holder inside an argon-filled glove box and sealed with a Kapton film before measurements. Synchrotron XRD measurements were performed at beamline station BL17B1 of the Shanghai Synchrotron Radiation Facility (SSRF) (λ = 0.6888 Å). The samples were sealed in a capillary tube. Synchrotron X-ray

computed tomography (XCT) measurements were performed at the BL13HB beamline of SSRF. The sample was sealed with a Kapton film before measurement. The energy of the X-ray beam was 30 keV and the visualization and segmentation of XCT images were performed using Avizo software. The melting behavior of S_8I_2 was determined by a differential scanning calorimeter (DSC Q2000) under a nitrogen flow rate of 50.0 ml min^{-1}. The Raman spectra were recorded on a multi-function confocal micro Raman imaging spectrometer (LabRAM Odyssey, Horiba France); calibration was performed with respect to single crystal silicon. The SEM imaging was performed with a field emission scanning electron microscope (Hitachi, Regulus8220, Japan). The X-ray photoelectron spectroscopy (XPS) measurement was performed using an AXIS Supra instrument (Kratos Analytical). The sample was transferred with an inert gas sample-transfer device to avoid air exposure. The cryo-TEM imaging, along with its SAED analysis, was performed on the JEOL-F200 instrument. The HAADF-STEM imaging and the corresponding EDX mapping and HRTEM imaging for S_8I_2/KB and S_8I_2/KB-$Li_{5.5}PS_{4.5}Cl_{1.5}$ composites (50 wt% of S_8I_2) were performed with a ThermoFisher Titan Themis G2 60-300 instrument.

EIS measurements

The ionic conductivities of solid electrolytes were measured by electrochemical impedance spectroscopy (EIS) using a Bio-Logic SP-200 electrochemical working station, with an amplitude of 10 mV and a frequency range of 7 MHz to 100 mHz, using 6 points per decade. The solid electrolyte powder was placed into a PEEK cylinder with a diameter of 10 mm. Two stainless steel rods were placed on opposite sides of the PEEK cylinder, cold pressed at 312 MPa for 3 min. Then the cell was placed into a custom-made stainless-steel casing with an applied pressure of ~ 90 MPa for the EIS measurements. The in situ EIS measurement was performed at different states of charge/discharge of the cell. Specifically, the cell was discharged/charged under a constant current of 0.2 C until the voltage reached a predefined value, at which point the EIS was measured. This galvanostatic procedure was repeated until the completion of the discharge/charging process. The frequency was scanned over the range spanning 7 MHz to 100 mHz with an AC amplitude of 10 mV, using 6 points per decade. The testing temperature was 25 ± 1 °C.

Electronic conductivity and ionic conductivity measurements of electrodes

The electronic conductivity of the electrodes was obtained by the DC polarization with an ion-blocking configuration of Ti|electrode|Ti. A constant voltage of ± 0.1 V, ± 0.3 V, ± 0.4 V (or ± 0.5 V) was applied for 2 h, respectively, to allow the cell polarization to reach equilibrium on the Bio-Logic SP-200 electrochemical working station. The ionic conductivity of the electrodes was obtained by the DC polarization with an electron-blocking configuration of Ti|Cu|LiIn|$Li_{5.5}PS_{4.5}Cl_{1.5}$|electrode|$Li_{5.5}PS_{4.5}Cl_{1.5}$|InLi|Cu|Ti. A constant voltage of 0.6 V was applied and held for 2 h to allow the cell polarization to reach equilibrium on the Bio-Logic SP-200 electrochemical working station. The testing temperature was 25 ± 1 °C.

XANES

The operando I K-edge XANES study was performed at the Sinopec E beamline BL04W at the Shanghai Synchrotron Radiation Facility (SSRF). The cell was prepared in an argon-filled glovebox (H_2O < 0.1ppm, O_2 < 0.1 ppm) using the S_8I_2/KB-$Li_{5.5}PS_{4.5}Cl_{1.5}$ positive electrode (30 wt% S_8I_2), a $Li_{5.5}PS_{4.5}Cl_{1.5}$ electrolyte separator layer and an In/InLi negative electrode with the Be window serving as the positive electrode current collector. The cell was measured by cycling at 0.19 mA cm^{-2} (0.2 C) and at 25 ± 1 °C under a pressure of ~ 30 MPa. The measurement uses the focusing mode with a Si (311) monochromator and fluorescence detection mode using a 36-element high-purity germanium solid-state detector. The Be window with a diameter of 5.5 mm was used to enhance X-ray penetration while maintaining the applied stacking pressure. The S K-edge XANES experiments were carried out at the 4B7A beamline of Beijing Synchrotron Radiation Facility (BSRF), using a Si (111) crystal monochromator. The measurements were collected in fluorescence mode. The S_8I_2/KB positive electrodes at varied states of charge (pristine, first charge to 3.2 V, first discharge to 1.4 V, and second charge to 3.2 V) and the references were sealed with a Kapton film to avoid exposure to air. Athena software was used to calibrate and normalize the XANES spectra.

TOF-SIMS measurements

The TOF-SIMS measurements were conducted with a PHI nano TOF II (ULVAC-PHI). Sample preparation and testing process were carried out according to the standard T/SHPTA 035 − 2023. Surface measurements and depth profiling of positive electrodes at varied states of charge were performed. During the sample transfer, a specialized transfer vessel that comes with the instrument was used, allowing direct transfer of the sample from the glove box to the TOF-SIMS vacuum chamber without exposure to ambient air. Surface measurements were performed in spectrometry mode, using Bi_3^{++} ions with an energy of 30 keV as primary ion species. Five mass spectra for each sample were recorded in negative ion mode at different locations on the surface with an area of 100 × 100 μm^2. For the depth profiling, sputter etching was conducted using an Ar^+ beam (3 kV 100 nA). A 50 × 50 μm^2 surface area was analyzed, with the sputtering area of 400 × 400 μm^2. Data evaluation was carried out with TOF-DR 3.0 software (ULVAC-PHI).

Differential electrochemical mass spectrometry (DEMS) measurements

A cell configured as In/InLi|LPSCl|S_8I_2/KB-$Li_{5.5}PS_{4.5}Cl_{1.5}$ with S_8I_2/KB-$Li_{5.5}PS_{4.5}Cl_{1.5}$ as the positive electrode was assembled to detect the I-related signal. A high S_8I_2 loading of ~ 9.7 mg $cm^{-2}_{S/I}$ was used for the cell. Prior to cycling, a 10 h rest period was implemented to stabilize the DEMS cell and to ensure a proper background for the mass spectrometer. The testing temperature was maintained at 45 ± 1 °C with an effort to promote sublimation of iodine. Helium was used as the carrier gas flowing through the cell at a controlled rate of 2.5 mL/min. Due to the limited mass range of DEMS (m/z < 200), the signal at m/z 254 (i.e., I_2) could not be directly observed. Since iodine is a solid with limited room temperature vapor pressure (35 Pa), only a small fraction of the formed iodine is expected to vaporize from the positive electrode, decreasing the measurement signal/noise ratio compared to the detection of gases. Furthermore, due to the compactness and solid-state nature of the positive electrode, the iodine is buried within the positive electrode, reducing the fraction of escaped iodine due to assumably closed porosity even further and likely delaying the observation of iodine (which accounts for the delay of m/z 127 peak here).

Data availability

The data generated in this study are included in the paper and the Supplementary Information. Source data are provided in this paper.

References

1. Liu, R. et al. Establishing reaction networks in the 16-electron sulfur reduction reaction. *Nature* **626**, 98–104 (2024).
2. Li, H. et al. Developing high-power Li||S batteries via transition metal/carbon nanocomposite electrocatalyst engineering. *Nat. Nanotechnol.* **19**, 792–799 (2024).
3. Zhou, G., Chen, H. & Cui, Y. Formulating energy density for designing practical lithium–sulfur batteries. *Nat. Energy.* **7**, 312–319 (2022).

4. Zheng, Z. J., Ye, H. & Guo, Z. P. Recent progress on pristine metal/covalent-organic frameworks and their composites for lithium–sulfur batteries. *Energy Environ. Sci.* **14**, 1835 (2021).
5. Pang, Q., Liang, X., Kwok, C. Y. & Nazar, L. F. Advances in lithium–sulfur batteries based on multifunctional cathodes and electrolytes. *Nat. Energy* **1**, 16132 (2016).
6. Meng, Y. S., Srinivasan, V. & Xu, K. Designing better electrolytes. *Science* **378**, 1065 (2022).
7. Seh, Z. W., Sun, Y., Zhang, Q. & Cui, Y. Designing high-energy lithium–sulfur batteries. *Chem. Soc. Rev.* **45**, 5605 (2016).
8. Zhao, C. et al. A high-energy and long-cycling lithium–sulfur pouch cell via a macroporous catalytic cathode with double-end binding sites. *Nat. Nanotechnol* **16**, 166–173 (2021).
9. Li, M. et al. A lithium–sulfur battery using a 2D current collector architecture with a large-sized sulfur host operated under high areal loading and low E/S Ratio. *Adv. Mater.* **30**, 1804271 (2018).
10. Pan, H. et al. Non-encapsulation approach for high-performance Li–S batteries through controlled nucleation and growth. *Nat. Energy* **2**, 813–820 (2017).
11. Shi, P. et al. A dielectric electrolyte composite with high lithium-ion conductivity for high-voltage solid-state lithium metal batteries. *Nat. Nanotechnol.* **18**, 602–610 (2023).
12. Ning, Z. et al. Dendrite initiation and propagation in lithium metal solid-state batteries. *Nature* **618**, 287–293 (2023).
13. Wang, L. et al. High-energy all-solid-state lithium batteries enabled by Co-free $LiNiO_2$ cathodes with robust outside-in structures. *Nat. Nanotechnol.* **19**, 208–218 (2024).
14. Ohno, S. & Zeier, W. G. Toward practical solid-state lithium–sulfur batteries: challenges and perspectives. *Acc. Mater. Res.* **2**, 869–880 (2021).
15. Gao, X. et al. All-solid-state lithium–sulfur batteries enhanced by redox mediators. *J. Am. Chem. Soc.* **143**, 18188–18195 (2021).
16. Kim, J. T. et al. Manipulating Li_2S_2/Li_2S mixed discharge products of all-solid-state lithium sulfur batteries for improved cycle life. *Nat. Commun.* **14**, 6404 (2023).
17. Pan, H. et al. Carbon-free and binder-free Li-Al alloy anode enabling an all-solid-state Li-S battery with high energy and stability. *Sci. Adv.* **8**, eabn4372 (2022).
18. Wang, S. et al. Thermal stability between sulfide solid electrolytes and oxide cathode. *ACS Nano* **16**, 16158–16176 (2022).
19. Janek, J. & Zeier, W. G. Challenges in speeding up solid-state battery development. *Nat. Energy* **8**, 230–240 (2023).
20. Yang, X., Luo, J. & Sun, X. Towards high-performance solid-state Li–S batteries: from fundamental understanding to engineering design. *Chem. Soc. Rev.* **49**, 2140–2195 (2020).
21. Dewald, G. F., Ohno, S., Hering, J. G. C., Janek, J. & Zeier, W. G. Analysis of charge carrier transport toward optimized cathode composites for All-Solid-State Li–S Batteries. *Batter. Supercaps* **4**, 183–194 (2021).
22. Bradbury, R. et al. Visualizing reaction fronts and transport limitations in solid-state Li–S batteries via operando neutron imaging. *Adv. Energy Mater* **13**, 2203426 (2023).
23. Han, F. et al. High-performance all-solid-state lithium–sulfur battery enabled by a mixed-conductive Li_2S nanocomposite. *Nano Lett.* **16**, 4521–4527 (2016).
24. Suzuki, K. et al. Composite sulfur electrode prepared by high-temperature mechanical milling for use in an all-solid-state lithium–sulfur battery with a $Li_{3.25}Ge_{0.25}P_{0.75}S_4$ electrolyte. *Electrochim. Acta* **258**, 110–115 (2017).
25. Wang, D. et al. Realizing high-capacity all-solid-state lithium-sulfur batteries using a low-density inorganic solid-state electrolyte. *Nat. Commun.* **14**, 1895 (2023).
26. Zhu, Y. et al. Uncoordinated chemistry enables highly conductive and stable electrolyte/filler interfaces for solid-state lithium–sulfur batteries. *Proc. Natl. Acad. Sci. USA* **120**, e2300197120 (2023).
27. Yamaguchi, H. et al. Local structure of amorphous sulfur in carbon–sulfur composites for all-solidstate lithium-sulfur batteries. *Commun. Chem.* **8**, 10 (2025).
28. Yan, H. et al. In situ generated Li_2S–C nanocomposite for high-capacity and long-life all-solid-state lithium sulfur batteries with ultrahigh areal mass loading. *Nano Lett.* **19**, 3280–3287 (2019).
29. Kwok, C. Y. et al. High-performance all-solid-state Li_2S batteries using an interfacial redox mediator. *Energy Environ. Sci.* **16**, 610–618 (2023).
30. Hakari, T., Hayashi, A. & Tatsumisago, M. Li_2S-based solid solutions as positive electrodes with full utilization and superlong cycle life in all-solid-state Li/S batteries. *Adv. Sustain. Syst.* **1**, 1700017 (2017).
31. Xu, R. et al. Cathode-supported all-solid-state lithium–sulfur batteries with high cell-level energy density. *ACS Energy Lett.* **4**, 1073–1079 (2019).
32. Zhou, J. et al. Healable and conductive sulfur iodide for solid-state Li–S batteries. *Nature* **627**, 301–305 (2024).
33. Wan, H., Wang, Z., Zhang, W., He, X. & Wang, C. Interface design for all-solid-state lithium batteries. *Nature* **623**, 739–744 (2023).
34. Liu, M. et al. Improving Li-ion interfacial transport in hybrid solid electrolytes. *Nat. Nanotechnol.* **17**, 959–967 (2022).
35. Tan, D. H. S. et al. Carbon-free high-loading silicon anodes enabled by sulfide solid electrolytes. *Science* **373**, 1494–1499 (2021).
36. Liu, J. et al. Pathways for practical high-energy long-cycling lithium metal batteries. *Nat. Energy* **4**, 180–186 (2019).
37. Pang, Q. et al. Fast-charging aluminium–chalcogen batteries resistant to dendritic shorting. *Nature* **608**, 704–711 (2022).
38. Xu, J. et al. Electrolyte design for Li-ion batteries under extreme operating conditions. *Nature* **614**, 694–700 (2023).
39. Schwietert, T. K. et al. Clarifying the relationship between redox activity and electrochemical stability in solid electrolytes. *Nat. Mater.* **19**, 428–435 (2020).
40. Ye, L. & Li, X. A dynamic stability design strategy for lithium metal solid state batteries. *Nature* **593**, 218–222 (2021).
41. Yin, Y. C. et al. A $LaCl_3$-based lithium superionic conductor compatible with lithium metal. *Nature* **616**, 77–83 (2023).
42. Lu, Y. C. et al. Lithium–oxygen batteries: bridging mechanistic understanding and battery performance. *Energy Environ. Sci.* **6**, 750 (2013).
43. Aurbach, D., McCloskey, B. D., Nazar, L. F. & Bruce, P. G. Advances in understanding mechanisms underpinning lithium–air batteries. *Nat. Energy* **1**, 16128 (2016).
44. Liu, T. et al. Cycling Li-O_2 batteries via LiOH formation and decomposition. *Science* **350**, 530–533 (2015).
45. Zhu, Z. et al. Anion-redox nanolithia cathodes for Li-ion batteries. *Nat. Energy* **1**, 16111 (2016).
46. Meini, S., Elazari, R., Rosenman, A., Garsuch, A. & Aurbach, D. The use of redox mediators for enhancing utilization of Li_2S cathodes for advanced Li–S battery systems. *J. Phys. Chem. Lett.* **5**, 915–918 (2014).
47. Liu, F. et al. Dual redox mediators accelerate the electrochemical kinetics of lithium-sulfur batteries. *Nat. Commun.* **11**, 5215 (2020).
48. Song, H. et al. All-solid-state Li–S batteries with fast solid–solid sulfur reaction. *Nature* **637**, 846–853 (2025).
49. Okamoto, H. I.-S. Iodine-Sulfur). *J. Phase Equil.* **21**, 109 (2000).
50. Lu, K. et al. A rechargeable iodine-carbon battery that exploits ion intercalation and iodine redox chemistry. *Nat. Commun.* **8**, 527 (2017).
51. De Rosa, C., Park, C., Thomas, E. & Lotz, B. Microdomain patterns from directional eutectic solidification and epitaxy. *Nature* **405**, 433–437 (2000).
52. Hecht, U., Eiken, J., Akamatsu, S. & Bottin-Rousseau, S. Phase boundary anisotropy and its effects on the maze-to-lamellar transition in a directionally solidified Al–Al_2Cu eutectic. *Acta Mater* **170**, 268–277 (2019).

53. Wang, S. et al. Lithium argyrodite as solid electrolyte and cathode precursor for solid-state batteries with long cycle life. *Adv. Energy Mater.* **11**, 2101370 (2021).
54. Holmes, C. F. The lithium/iodine-polyvinylpyridine battery–35 years of successful clinical use. *ECS Trans.* **6**, 1 (2007).
55. Ahn, S. et al. Why charging Li–air batteries with current low-voltage mediators is slow and singlet oxygen does not explain degradation. *Nat. Chem.* **15**, 1022–1029 (2023).
56. Bergner, B. J., Schürmann, A., Peppler, K., Garsuch, A. & Janek, J. TEMPO: A mobile catalyst for rechargeable Li-O_2 batteries. *J. Am. Chem. Soc.* **136**, 15054–15064 (2014).
57. Cheng, D. et al. A free-standing lithium phosphorus oxynitride thin film electrolyte promotes uniformly dense lithium metal deposition with no external pressure. *Nat. Nanotechnol.* **18**, 1448–1455 (2023).

Acknowledgements

The authors thank the Materials Processing and Analysis Center of Peking University. The authors thank the beamline station 4B7A at the Beijing Synchrotron Radiation Facility (BSRF) for the XANES measurement and the Sinopec E beamline BL04W at the Shanghai Synchrotron Radiation Facility (SSRF) for operando I K-edge XANES spectra. The authors thank Prof. G. Peng and the beamline station BL13HB at SSRF for the synchrotron XCT measurement. The authors thank the beamline station BL17B1 at SSRF for the synchrotron radiation XRD measurement and the beamline station BL14W1. The authors acknowledge Prof. X. Su and Prof. Y. Hu at SSRF for their discussion and assistance with data analysis. The authors thank the Experimental Center of Advanced Materials at Beijing Institute of Technology for TOF-SIMS measurements.

Author contributions

Q.P. and H.S. conceived the concept and designed the experiments. H.S. conducted the materials synthesis with the help of J.M., M.H, Y.M., and Y.L. H.S. performed the physiochemical characterizations and electrochemical measurements with the help of K.S., Y.Y., W.S., Z.X., and M.B.S. H.S., K.S., and X.H. performed the S K-edge XANES synchrotron measurements with the guidance and contribution from C.M. and L.Z. R.Z., K.M., P.H., J.J., and T.B. conducted the DEMS measurements. C.Z., F.L., H.W., J.W., and P.G. carried out the TEM measurements. T.S. performed the TOF-SIMS measurement with data analysis contribution from K.M. and J.J. M.S. contributed to the conductivity measurements. X.G., M.L., and Y.W. contributed to the I K-edge XANES measurements. All authors participated in the discussion of the results and contributed to the data analysis. H.S. and Q.P. wrote the manuscript with contributions from all authors. Q.P. supervised the work.

Funding

Q.P. discloses support for the research of this work from the National Key R&D Program of China (No. 2021YFB2500200), the Beijing Natural Science Foundation (No. Z220020), the "U35 Pei Miao Funding Program" of Changping District, Beijing (Grant No. CHPU35202502002), the National Natural Science Foundation of China (No. 2252500158; No. 92372115), the China National Petroleum Corporation-Peking University Strategic Cooperation Project of Fundamental Research and the New Cornerstone Science Foundation through the XPLORER PRIZE. K.M. and J.J. disclose support for the research of this work from the BMBF (Bundesministerium für Bildung und Forschung, Germany) through the project SOLiS (No. 03XP0395D). H.S. discloses support for the research of this work from the China Postdoctoral Science Foundation (No. 2026T190002).

Competing interests

The authors declare no competing interests.

Additional information

Supplementary information The online version contains supplementary material available at https://doi.org/10.1038/s41467-026-78042-6.

Correspondence and requests for materials should be addressed to Quanquan Pang.

Peer review information *Nature Communications* thanks the anonymous reviewers for their contribution to the peer review of this work. A peer review file is available.

Reprints and permissions information is available at http://www.nature.com/reprints

Publisher's note Springer Nature remains neutral with regard to jurisdictional claims in published maps and institutional affiliations.

Open Access This article is licensed under a Creative Commons Attribution-NonCommercial-NoDerivatives 4.0 International License, which permits any non-commercial use, sharing, distribution and reproduction in any medium or format, as long as you give appropriate credit to the original author(s) and the source, provide a link to the Creative Commons licence, and indicate if you modified the licensed material. You do not have permission under this licence to share adapted material derived from this article or parts of it. The images or other third party material in this article are included in the article's Creative Commons licence, unless indicated otherwise in a credit line to the material. If material is not included in the article's Creative Commons licence and your intended use is not permitted by statutory regulation or exceeds the permitted use, you will need to obtain permission directly from the copyright holder. To view a copy of this licence, visit http://creativecommons.org/licenses/by-nc-nd/4.0/.

© The Author(s) 2026

[1]Beijing Key Laboratory for Theory and Technology of Advanced Battery Materials, School of Materials Science and Engineering, Peking University, Beijing, China. [2]Battery and Electrochemistry Laboratory (BELLA), Institute of Nanotechnology, Karlsruhe Institute of Technology (KIT), Karlsruhe, Germany. [3]International Center for Quantum Materials, Collaborative Innovation Center of Quantum Matter, Peking University, Beijing, China. [4]Institute of Physical Chemistry and Center for Materials Research, Justus Liebig University Giessen, Giessen, Germany. [5]State Key Laboratory of Advanced Technology for Materials Synthesis and Processing, School of Materials Science and Engineering, Wuhan University of Technology, Wuhan, China. [6]Experimental Center of Advanced Materials, School of Materials Science & Engineering, Beijing Institute of Technology, Beijing, China. [7]Institute of High Energy Physics, Chinese Academy of Sciences, Beijing, China. [8]Institute for Materials Research (IMO-imomec), UHasselt, Martelarenlaan 42, Hasselt, Belgium. [9]Shanghai Synchrotron Radiation Facility, Zhangjiang Laboratory, Shanghai Advanced Research Institute, Chinese Academy of Sciences, Shanghai, China.
✉e-mail: qqpang@pku.edu.cn